nature electronics

ARTICLES

https://doi.org/10.1038/s41928-021-00656-z

Check for updates

Optical activation and detection of charge transport between individual colour centres in diamond

Artur Lozovoi[1], Harishankar Jayakumar[1], Damon Daw[1], Gyorgy Vizkelethy[2], Edward Bielejec[2], Marcus W. Doherty[3], Johannes Flick[4] and Carlos A. Meriles[1,5]✉

Understanding the capture of charge carriers by colour centres in semiconductors is important for the development of novel forms of sensing and quantum information processing, but experiments typically involve ensemble measurements, often impacted by defect proximity. Here we show that confocal fluorescence microscopy and magnetic resonance can be used to induce and probe charge transport between individual nitrogen-vacancy centres in diamond at room temperature. In our experiments, a 'source' nitrogen vacancy undergoes optically driven cycles of ionization and recombination to produce a stream of photogenerated carriers, one of which is subsequently captured by a 'target' nitrogen vacancy several micrometres away. We use a spin-to-charge conversion scheme to encode the spin state of the source colour centre into the charge state of the target, which allows us to set an upper bound to carrier injection from other background defects. We attribute our observations to the action of unscreened Coulomb potentials producing giant carrier capture cross-sections, orders of magnitude greater than those measured in ensembles.

Although point defects in solids have often been viewed as a problem in semiconductor technologies, recent work has shown that they can be of use in nanoscale sensing and solid-state quantum information processing[1,2]. Among a rapidly growing list of defects with attractive physical properties[3], select spin-active colour centres in wide-bandgap semiconductors—including diamond[4], silicon carbide[5] or hexagonal boron nitride[6]—are of particular interest due to their favourable optical and magneto-optical properties. Given the impact of the charge state on defect spin and photon emission properties, understanding defect photoionization[7] and carrier trapping[8] deep inside the crystal[9–11] and near the surface[12,13] is essential. Charge control methods are also being explored to provide a route to reduced spectral diffusion[14,15], alternative forms of electric-field sensing[16], super-resolution imaging[17,18] and Stark tuning of the optical transitions through the photoexcitation of trapped charges[19]. Furthermore, electroluminescence produced by electron–hole recombination at individual colour centres has been observed at room temperature in an all-diamond diode structure[20].

The interplay between the colour centre's spin and charge states is particularly interesting, and it has already been exploited to, for example, enhance detection sensitivity[21–23], create decoherence-protected qubit states[24], and store and retrieve classical information[25]. Recent experiments have used spin-to-charge conversion (SCC) protocols to demonstrate the photoelectrical detection of magnetic resonance from individual colour centres in diamond[26–28] and silicon carbide[29]. Similarly, spin-based electrometry from a probe colour centre has been used to monitor changes in the local charge environment[30]. Spin-encoded photogenerated carriers propagating from source point defects to target point defects have also been proposed as a bus to communicate pairs of distant qubits in a solid-state chip[31].

In this Article, we show that high-energy ion implantation can be used to engineer spatial patterns of nitrogen-vacancy (NV) centres in pristine bulk diamond. With the help of multicolour confocal microscopy and optically detected magnetic resonance, we investigate the photoionization and carrier-trapping properties of small NV sets, down to the limit of individual colour centres. We focus on the transport of carriers between physically separate source and target defects, which we selectively address via independent laser beams. We also use spin-dependent ionization to filter out carriers stemming from source NVs (as opposed to other concomitant defects in the sample) and show that they are dominant in establishing carrier transport. By lowering the number of source and target defects to the level of individual NVs, we are able to probe inter-defect carrier transport as a means to directly measure NV carrier-trapping cross-sections.

Carrier transport between individual colour centres

We conduct our experiments in a type IIa diamond with an intrinsic nitrogen concentration of $\lesssim$5 parts per billion (ppb). To engineer NV centres at select locations, we first use a focused ion beam from a tandem accelerator to implant nitrogen ions ~10 μm deep into the crystal (Fig. 1a), which we subsequently convert into NV centres via sample annealing[32,33]. Carriers photoinjected from defects at this depth remain within the bulk crystal during inter-defect propagation, thus making our observations free from surface effects. Further, the ability to focus the ion beam over ~1-μm-diameter spots gives us the opportunity to engineer virtually arbitrary implantation geometries (Methods and Extended Data Fig. 1). Figure 1b shows a simple case, in the form of an NV grid here; by varying the ion beam fluence, we produce arrays with variable colour-centre content often leading to the formation of pairs of NVs micrometres apart. Figure 1c

[1]Department of Physics, CUNY—City College of New York, New York, NY, USA. [2]Sandia National Laboratories, Albuquerque, NM, USA. [3]Laser Physics Centre, Research School of Physics, Australian National University, Canberra, Australian Capital Territory, Australia. [4]Center for Computational Quantum Physics, Flatiron Institute, New York, NY, USA. [5]Graduate Center, CUNY, New York, NY, USA. ✉e-mail: cmeriles@ccny.cuny.edu

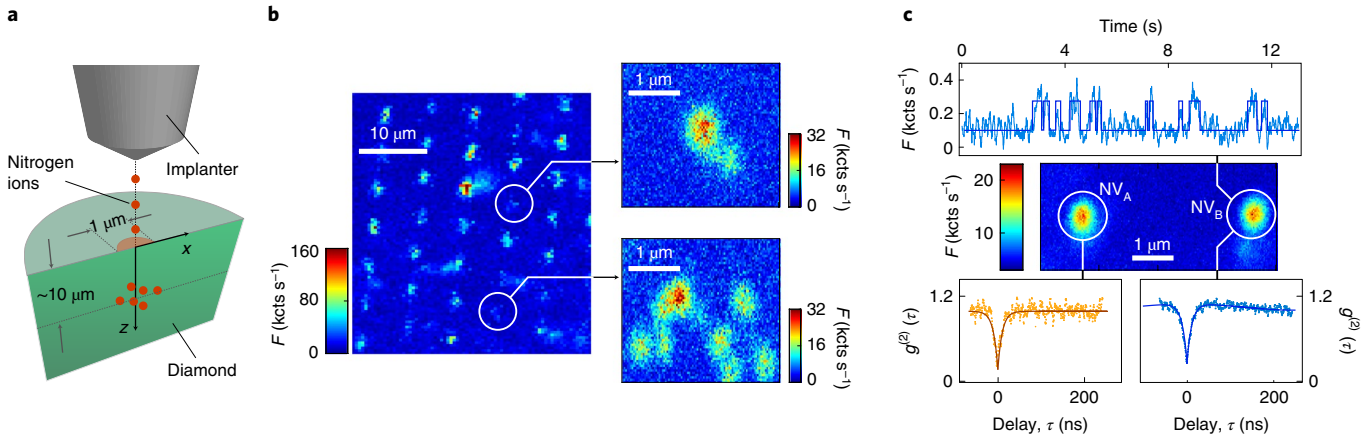

Fig. 1 | Engineering NV spatial patterns. a, Ion implantation geometry. We accelerate N^+ ions using a tandem accelerator focused over an ~1-μm-diameter spot on the diamond surface. **b**, NV fluorescence image of the implanted grid under 520 nm/1 mW excitation. Zoomed-in images on the right show individual NVs. *F*, fluorescence; kcts, kilocounts. **c**, Confocal fluorescence image of individual NV centres 4 μm apart under 520 nm/0.5 mW excitation. In our experiments, photogenerated carriers diffuse from NV_A to NV_B (referred to as the 'source' and 'target' NVs, respectively). The bottom insets show the individual photon autocorrelation curves $g^{(2)}(\tau)$. The top time trace shows fluorescence blinking from NV_B, as expected for single-photon emitters.

shows one such example, as demonstrated by photon autocorrelation and fluorescence–time trace measurements at each site.

An initial demonstration of carrier propagation between individual colour centres is presented in Fig. 2. In these experiments, carrier photogeneration is derived from NV charge-state interconversion during prolonged green 520 nm optical excitation (Fig. 2a); electron injection into the conduction band emerges from NV^- ionization, whereas holes are produced during NV^0 recombination[8,9]. Using suitable bandpass filters to separate NV^- from NV^0 emission[34], we expose inter-defect carrier propagation—relying on self-diffusion in this case, as shown below—by monitoring the fluorescence from NV_B (Fig. 2b). Initially prepared in the negatively charged 'bright' state, the target NV turns to 'dark' on the capture of a hole produced by NV_A (acting as the carrier source here; Fig. 2c). Note that although the same (or comparable) number of electrons and holes are produced during a green laser park, Coulomb attraction makes the hole-capture cross-section of NV^- dominant[8], thus leading to a net fluorescence change. Further, given the relatively low defect content, this change is infinitely long-lived in the dark[25] and thus can be subsequently imaged with the help of a 594 nm beam (orange illumination excites only NV^- fluorescence[7]; Fig. 2a). Note that since some NV^0 recombinations take place at 594 nm (Methods), the probe intensity is chosen so as to optimize the photon count without impacting the NV charge state.

Figure 2d shows the integrated fluorescence in the area surrounding NV_B as a function of park time t_P for some examples of green laser powers. For sufficiently long park times, the integrated fluorescence at the target site decays to the background levels, consistent with prior observations in ensembles[9]. Capitalizing on the photoluminescence decay curves to extract the NV^- hole capture rates τ^{-1} at various powers, we find a quadratic dependence (Fig. 2d, inset), as expected for two-photon processes governing charge interconversion in the source NV (ref. [7]) (Fig. 2a and Extended Data Fig. 2). In each case, the time scale $\tau \approx 4\pi d^2/(k_h \sigma_h)$ of the process—in the order of a few hundred milliseconds depending on the laser power—arises from an interplay between the target hole capture cross-section σ_h (see below), the inter-defect distance d (~4 μm in this case) and the unit-time number of photogenerated holes k_h (produced by the source NV as it cycles from negative to neutral and back under continuous green illumination). The latter can be related to the NV ionization and recombination rates as $k_h = \left(k_{ion}^{-1} + k_{rec}^{-1}\right)^{-1}$. Since $\sigma_h/4\pi d^2$ is the fractional area associated with the target NV, τ can be intuitively interpreted as the time during which enough holes have been generated to ensure a capture event with almost 100% probability.

We note that the time-averaged fluorescence from NV_A remains unchanged as a function of the illumination duration or laser power, consistent with stochastic cycles of ionization and recombination under continuous green excitation (Extended Data Fig. 3a,b). By contrast, the red excitation of the source induces rapid conversion of NV_A into the neutral, dark state with no bleaching in the fluorescence from NV_B, as anticipated for a one-directional ionization process that entails no hole injection (Extended Data Fig. 3c,d). In combination, these observations suggest that photogenerated carriers predominantly originate from NV_A (as opposed to other neighbouring defects)—an important consideration addressed in more detail below.

SCC as a carrier source filter

Although a large fraction of the implanted nitrogen ions converts into NV centres after sample annealing[33], residual defects—for example, in the form of substitutional nitrogen or 'P1 centres'—may coexist, arguably serving as parasitic charge injection sources. To selectively filter out contributions stemming from NV centres alone, we implement the protocol shown in Fig. 3a: following charge and spin initialization, we subject the source NV to cycles of microwave (MW) excitation and simultaneous green (520 nm) and red (632 nm) excitation with relative powers adapted for optimal NV^- ionization[35,36]. Similar SCC schemes have been successfully utilized in the recent past, for both individual NVs and small ensembles[22,35,37]. Briefly, resonant MW driving of the zero-field transition in the NV ground electronic state (where the spin number is $S=1$) counters optical spin pumping into the $m_S=0$ projection of the triplet, hence increasing the chance of intersystem crossing into the singlet manifold (Fig. 3b). The associated shelving that accompanies this crossing impacts the timing in the optical excitation cycle of NV^- and thus effectively lowers its two-step ionization rate[26–29]. Correspondingly, there is a reduction in the number of photogenerated holes approaching the target colour centre and thus a relative increase in its emitted fluorescence.

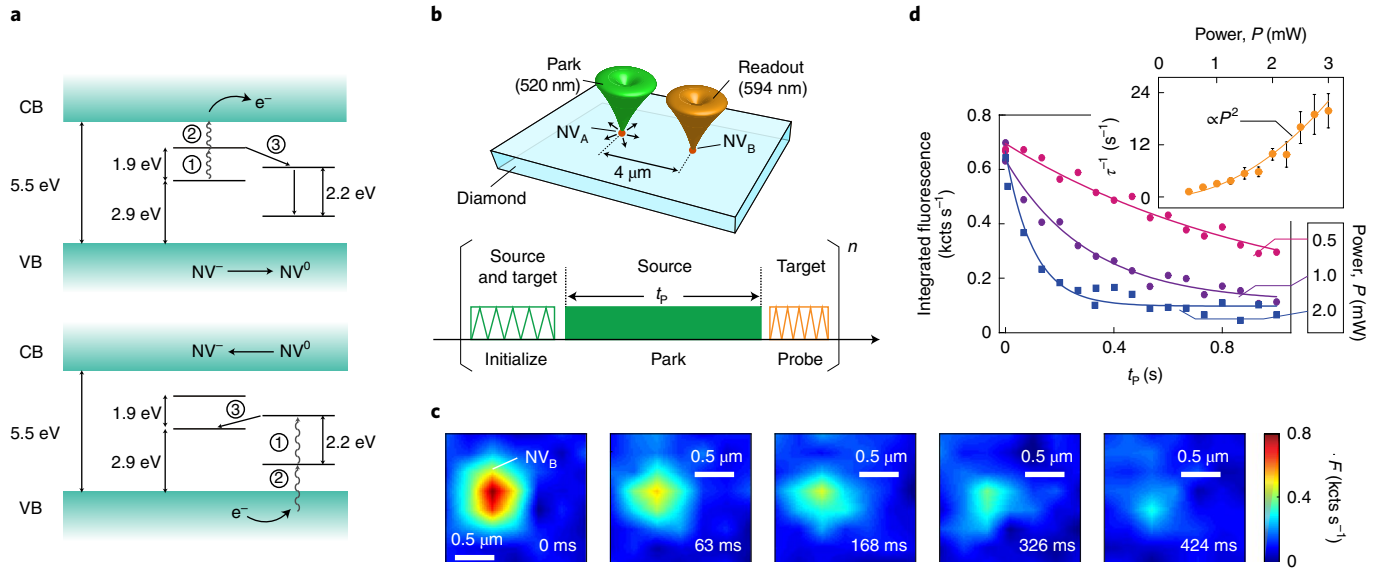

Fig. 2 | Controlling charge transport between source and target colour centres. a, Schematic of NV photochromism under optical (~460–637 nm) excitation. Top (bottom): NV^- ionization (NV^0 recombination). In each case, steps (1)–(3) describe the successive absorption of two photons followed by NV charge transformation and injection of an electron (hole) into the conduction band (CB) (valence band (VB)), respectively. **b**, Experimental geometry (top) and charge transfer protocol (bottom); the green (orange) zigzag line indicates a charge initialization (readout) scan at 520 nm and 2.5 mW (594 nm and 7 μW). The solid green block indicates laser parking at 520 nm and 2.5 mW at NV_A. **c**, Fluorescence images of NV_B on application of the protocol in **b** for variable park durations t_P (lower right corner). Each image results from a 7 × 7 pixel, 594 nm beam scan (7 μW, 10 ms per pixel); for clarity, we use linear colour interpolation between the sites. **d**, Integrated fluorescence in a 1.5 × 1.5 μm² area containing NV_B as a function of t_P for variable park powers; solid lines indicate exponential fits. Inset: unit-time charge conversion probability τ^{-1} of NV_B as a function of the park power at NV_A. Error bars indicate standard deviation. In these experiments, the total number of repeats is $n = 10^2$.

We isolate the impact of the NV_A-produced carriers by referencing the NV_B fluorescence to the response with no MW. To quantify the effect, we measure the non-local SCC contrast $\mathbb{C}_{SCC}^{(nol)} = \Delta F(\nu)/\Delta F_{Ref}$, where $\Delta F(\nu) = F_{On}(\nu) - F_{Off}$ is the fluorescence change with and without MW at frequency ν, and $\Delta F_{Ref} = F_{Ref} - F_{Off}$ with F_{Ref} denoting the target NV fluorescence in the absence of optical excitation at the source. Experimentally, we find the maximum contrast when MW is on resonance with the NV^- crystal-field transition (Fig. 3c); by monitoring the response as a function of the MW frequency, we reconstruct what amounts to an ancilla-detected NV^- spin resonance spectrum[38] (Fig. 3d). Unlike in regular optically detected magnetic resonance experiments (Fig. 3d, inset), the fluorescence change is positive, consistent with the effectively lower carrier photogeneration at the source. Since the local SCC contrast in NV_A reaches up to 30% (Extended Data Fig. 4), the observed fluorescence change in NV_B indicates that not less than 75% of the trapped photogenerated carriers stem from the source NV. We emphasize that this is a lower bound because, for example, background holes from NV_A produced during the spin initialization time t_P can lower the observed spin contrast. For completeness, we mention that virtually identical results are derived from carrier transport experiments between islands comprising few NVs each (Extended Data Fig. 5). Externally applied fields can be exploited to gain some control on the transport process (Methods and Extended Data Fig. 6), although the formation of space-charge fields can substantially complicate the dynamics at play[36].

Modelling the capture process

An interesting pending question relates to the impact of inter-defect distance d on the carrier capture probability. In the simplest picture, probability distribution describing the photogenerated carriers radially evolves from the source NV (Fig. 4a), thus making the carrier capture probability proportional to d^{-2}. To test this notion, we use the protocol shown in Fig. 2b to monitor the carrier transport between pairs of NVs separated by variable distances ranging from 2.5 to 9.5 μm (Fig. 4b). Figure 4c shows the results for a fixed park laser power and duration confirming the anticipated inverse square dependence. From the expression $\tau \approx 4\pi d^2/(k_h \sigma_h)$ introduced earlier and using $k_h = \left(k_{ion}^{-1} + k_{rec}^{-1}\right)^{-1} \approx 2 \times 10^5\,s^{-1}$ at the applied green laser power (1 mW), we find $\sigma_h \approx 3 \times 10^{-3}\,\mu m^2$; for the NV pair shown in Fig. 2, this roughly amounts to the equivalent of one capture out of 10^5 generated holes (Methods).

To rationalize our observations, we describe hole capture as a process that involves the formation of a bound exciton state featuring an electron localized at the NV core and an orbiting hole[20]. In this model that was recently invoked to interpret the absorption spectrum of neutral silicon-vacancy centres in diamond[39], eigenstates follow a hydrogenic sequence whose radii r_n grow with the square of the orbital quantum number n. Ab initio calculations support this model, although size limitations in the supercell restrict our analysis to the lower-energy orbital (whose energy slightly departs from that predicted by the hydrogenic series due to the finite size of charge distribution at the core; Methods and Extended Data Figs. 7 and 8).

Physically, hole capture takes place via a cascade process involving the consecutive emission of phonons[40]. By ensuring that the exciton's binding energy is comparable to the free hole thermal energy $\kappa_B T$ (~25 meV in our room-temperature experiments), we derive the trapping radius $r_t = e^2/(4\pi\varepsilon\kappa_B T) \approx 10$ nm, where e denotes the elementary charge, $\varepsilon = 5.7\varepsilon_0$ is the dielectric permittivity of diamond, κ_B denotes the Boltzmann's constant and T is the absolute temperature; correspondingly, we estimate the Onsager capture cross-section as $\sigma_{h,On} \approx \pi r_t^2 \approx 3 \times 10^{-4}\,\mu m^2$.

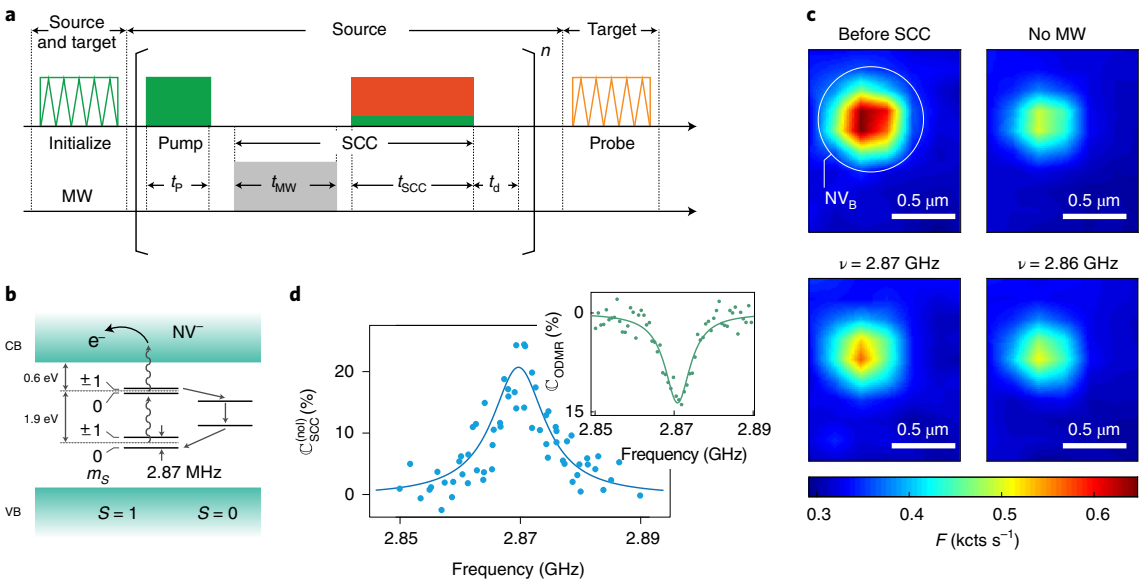

Fig. 3 | Filtering out NV-generated carriers. a, The SCC protocol. Green/red solid blocks indicate local laser excitation at 520 and 632 nm of NV_A (the source NV in this case); green and orange zigzag lines are laser scans at 520 and 594 nm, respectively. **b**, NV^- energy diagram including the zero-field splittings of the ground- and excited-state triplets ($S=1$) as well as the singlet ($S=0$) manifold levels. Intersystem crossing is more likely from the $m_S=\pm1$ states in the excited triplet, thus leading to a spin-dependent NV^- ionization rate. **c**, Top: confocal images of NV_B (the target NV) before (left) and after (right) the application of the protocol in **a** in the absence of MW. Bottom: on-resonance excitation at 2.87 GHz (left) reduces carrier generation at the source NV and thus diminishes bleaching of the target. For clarity, we use linear colour interpolation between the sites. **d**, Integrated fluorescence contrast $\mathbb{C}$ at the target NV as a function of the MW frequency. Top right inset shows the optically detected magnetic resonance spectrum of the source NV. In these experiments, $t_P=1.00\,\mu s$, duration of the SCC pulse $t_{SCC}=0.30\,\mu s$, MW pulse duration $t_{MW}=0.15\,\mu s$, delay time between consecutive cycles of SCC protocol $t_d=10.00$ ns and $n=5\times10^5$; the red laser power during SCC is 16 mW, whereas the green laser power is 200 μW during the initialization scan, t_{SCC} and t_P. All the other conditions are the same as in Fig. 2. $\mathbb{C}_{ODMR}$, optically detected magnetic resonance contrast.

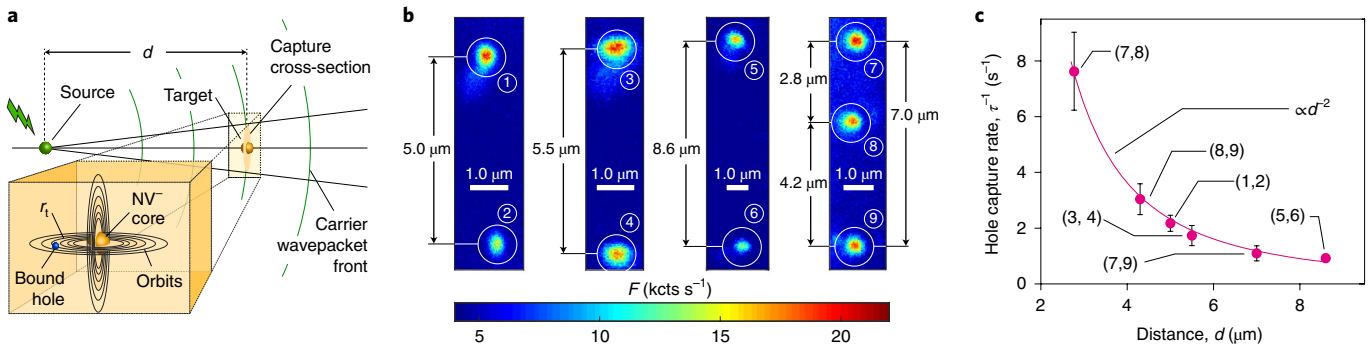

Fig. 4 | Photoinduced carrier transport between NVs at variable distances. a, Schematic of carrier-scattering dynamics. Assuming an initial wavepacket centred at the source, the carrier capture probability decreases approximately with the square of distance d to the target. Hole capture takes place via the formation of a transient-bound exciton characterized by the trapping radius r_t. **b**, To gauge the impact of distance on the carrier capture dynamics, we select a pair of target and source NVs from a discrete set, as shown in the fluorescence images (white circles). **c**, Hole capture rate τ^{-1} as a function of distance d; the solid line indicates an inverse square dependence. Indices in each pair denote the source and target NV sites in each measurement following the labels in **b**; the green laser power during these experiments is 1 mW, and all the other conditions are the same as in Fig. 2.

One possible key to the giant cross-section observed herein—several orders of magnitude greater than typical values considered in the literature[41]—is the lack of thermally activated carriers, which leads to the unscreened action of the Coulomb potential from a point defect. Equally important is high sample purity, favouring the transient formation of bound exciton orbitals with large radii. In a semiclassical picture, hole capture starts immediately after orbital formation via phonon-scattering processes in which the approaching carrier releases part of the kinetic energy gained as it accelerates towards the charged defect. For the present experimental conditions, the Langevin regime—where multiple collisions occur within the trapping radius—seems more appropriate because the carrier mean free path in room-temperature diamond amounts to ~15 nm (refs. [42,43]), comparable to r_t. Using the capture cross-section formula valid in this limit[40], we attain $\sigma_{h,On}=4.35\times10^{-3}\,\mu m^2$, close to the experimental value. We warn that this agreement can be partly fortuitous as the Langevin formula amounts to a crude approximation.

Conclusions

We have reported an approach to control and assess the transport of charge carriers between individual colour centres in diamond. Extending these experiments to include spin initialization of the

target NV or the photogenerated carrier[31] could be used to address the question of spin selectivity during trapping, as well as to determine the free carrier spin lifetime that is still unknown despite the near-ideal properties of diamond as a spintronics material[44,45]. Also of interest is the potential for local optical spectroscopy measurement designed to probe the higher-energy orbitals of a neutral NV; Rydberg states featuring 2 µm radii (corresponding to $n=25$) have already been observed in Cu_2O (ref. [46]).

Similarly attractive are extensions to low temperatures, where SCC can be implemented with near-unit fidelity[47], or in the presence of externally applied electric fields, provided space-charge effects can be used to an advantage[36]. Furthermore, by simultaneously monitoring the target and source fluorescence, it should be possible to time-correlate carrier photogeneration and capture. This class of heralding—applied to NVs or adapted to other neighbouring defects such as the P1 centre—could find use as a strategy towards distributing entanglement between remote spin qubits[31]. Increased hole capture probabilities could be attained by carrier confinement[48] (for example, via diamond nanobeams) or through the use of carrier lensing[49] in the limit of ballistic propagation. More generally, the ability to encode the spin state of a source qubit in the charge state of an ancilla defect (not necessarily paramagnetic) could prove useful to enhance the detection sensitivity of point defects with low quantum yield (such as rare-earth ions[38,50]) or with photon emission at impractical wavelengths (such as the neutral charge state of silicon vacancy in diamond[51]).

Methods

Experimental setup. The optical measurements throughout this work use a home-built confocal microscope with an oil-immersion objective (numerical aperture, 1.3) equipped with three continuous-wave diode lasers with emission at 520, 632 and 594 nm (Coherent); in all the cases, we reach a diffraction-limited illumination spot (diameter of the order of 0.5 µm). All the three laser beams are combined with the use of two dichroic mirrors (605 and 550 nm long-pass filters; Semrock) into a single-mode fibre (Thorlabs). The 520 and 632 nm lasers allow for fast pulsing (100 MHz), whereas the 594 nm beam is controlled via an acousto-optic modulator with switching times <30 ns (Isomet). A single-photon counting module based on an avalanche photodiode (Excelitas) is used for collection. A 650 nm long-pass dichroic mirror (Semrock) separates the excitation light from the detected photoluminescence, which is then coupled into a 25 µm multimode fibre (Thorlabs). This configuration proved to yield a higher count rate and sensitivity for the charge-state-based measurements presented herein, compared with a collection path with a single-mode fibre. Spin-resonance MW transitions are addressed through an omega-shaped strip-line antenna imprinted on an electronic board, also serving as the sample support. We displace the objective along the optical axis via a high-precision (<10 nm) piezoelectric nano-positioner (Edmund Optics). We use a time-correlated single-photon counting unit PicoHarp 300 (PicoQuant) in the Hanbury Brown–Twiss configuration for autocorrelation measurements. All the experiments are carried out under ambient conditions.

Sample preparation. We conduct our experiments in an electronic-grade [100] diamond crystal ($2.0\times2.0\times0.2$ mm^3) purchased from DDK, with an intrinsic nitrogen content of $\lesssim$5 ppb (which corresponds to an inter-nitrogen separation of $\gtrsim$200 nm). To engineer NV centres at select locations, we use a tandem ion accelerator at Sandia National Laboratory (New Mexico, USA), producing a 20 MeV ^{14}N beam with an ~1-µm-diameter focal spot (Extended Data Fig. 1a). Implantation patterns of different sizes, shapes and fluences were created using this system; some examples are shown in Extended Data Fig. 1b–d. From stopping and range of ions in matter (SRIM) calculations[52] (Extended Data Fig. 1e), we estimate that ions propagate for about 12 µm into the crystal before coming to a stop; the modelled lateral straggle amounts to 0.7 µm (a value that must be convoluted with the beam size, which is not considered here). The NV depth resulting from high-energy ion implantation ensures that the charges propagating between NVs are not affected by surface effects (for example, scattering or trapping by surface defects).

We set the beam fluence within the range of 1×10^8–5×10^{11} ions cm^{-2}, with the lowest bound corresponding to 2 ions per implantation spot (aimed at producing single-NV sites). Following implantation, we implement a six-step sample-annealing protocol[32], namely, (1) 20–400 °C ramp-up for 1 h, (2) 400 °C annealing for 4 h, (3) 400–800 °C ramp-up for 1 h, (4) 800 °C annealing for 2 h, (5) 800–1,200 °C ramp-up for 1 h and (6) 1,200 °C annealing for 2 h. Throughout the process, we maintain the vacuum level in the annealing chamber below 10^{-6} torr. Subsequently, we treat the sample with a tri-acid mixture (nitric, sulfuric and perchloric acids in 1:1:1 proportion) for 1 h to eliminate graphite and other impurities formed on the surface, as well as to provide oxygen termination.

A direct measurement of the fraction of nitrogen implants converting into NVs proved difficult because space-charge fields during implantation created instabilities in the beam fluence that cannot be accounted. We do find, however, areas in the low-fluence grid where sites show few NV centres (typically, one or none), hence suggesting the conversion efficiency is not far from typical values (of the order of 50% for bulk NVs[33]).

To experimentally determine the NV depth, we monitor the NV fluorescence as a function of the objective's z position along the optical axis; a single-mode 600–750 nm fibre (Thorlabs) is used in this measurement to attain the maximum axial resolution. Extended Data Fig. 1f shows the result for NV_A and NV_B (Fig. 1c): we identify the diamond surface from the initial fluorescence onset (black dashed line in Extended Data Fig. 1f) stemming from the reflected laser light (leaking into the detector despite the filters) as well as from surface-defect-induced fluorescence. From the position of the second fluorescence maximum, we determine a depth of ~10 and ~9 µm for NV_A and NV_B, respectively, slightly greater than—but still consistent with—the value obtained from SRIM calculations.

An extensive sample characterization shows that NV sites resulting from the highest beam fluences—which, unfortunately, included all ring-like geometries—feature a charge state that is rather insensitive to optical excitation. In particular, ionization into a neutral state proved difficult or short-lived, which suggests electron tunnelling from nearby traps, as observed previously[12]. On the contrary, we find that sites with lower NV density exhibit metastable (that is, infinitely lived) charge states that can be optically controlled. The experiments reported in this article are limited to this second class of sites.

Charge-state control of individual NVs. To properly interpret our carrier transport experiments, we first proceed to characterize the individual charge-state dynamics of the source and target NVs (Fig. 1c). Extended Data Fig. 2a shows our experimental protocol: we use consecutive green (520 nm) and orange (594 nm) laser pulses to initialize and subsequently transform the NV charge state; we then conduct an NV readout via a low-power orange pulse. Since strong green (orange) illumination preferentially prepares the NV in the negative (neutral) charge state, the ensuing orange (green) excitation pulse predominantly leads to NV^- ionization (NV^0 recombination). Note, however, that although one process or the other prevails depending on the laser wavelength[7], both are invariably present, meaning that an integrated analysis must be put in place to properly extract the underlying charge conversion rates (as shown below). On the other hand, orange excitation is known to have a comparatively lower impact on the NV charge state (a property that can be exploited to observe charge state jumps in real time; Fig. 1c), thus justifying the use of weak orange excitation for readout of the charge state.

To identify the fractional NV populations in either charge state, we plot our results in the form of histograms, each representing the probability distribution associated with fluorescence readouts for a given photon count. Extended Data Fig. 2b,c show some examples corresponding to alternative variants of the measurement protocol (as per the colour codes in the insets). In all the cases, we identify a bimodal dispersion whose low-count-rate (high-count-rate) peak reveals the fractional NV^0 (NV^-) population at a given time during the charge-conversion segment t_{Exc} of the protocol. We extract either relative population from a fit containing two Poissonian distributions with distinct average photon count rates. Extended Data Fig. 2b,c display the evolution of the NV^- population as a function of t_{Exc} under laser excitation at 520 and 594 nm, respectively. The former indicates the dynamics are dominated by NV^0 recombination, whereas the latter mainly signals NV^- ionization; in both instances, however, the charge conversion is partial, hence confirming the simultaneous presence of a counter mechanism.

Formally, we describe local NV charge conversion via a set of master equations, namely

$$\begin{aligned}\frac{dQ_-}{dt} &= -k_{ion}Q_- + k_{rec}Q_0\\ \frac{dQ_0}{dt} &= k_{ion}Q_- - k_{rec}Q_0\end{aligned} \quad (1)$$

Here Q_- and Q_0 denote the normalized NV^- and NV^0 populations, respectively, and k_{ion} and k_{rec} stand for the ionization and recombination rates under photoexcitation, respectively. With the simplifying assumption of full NV^- initialization under green excitation, the detailed balance set in equation (1) has the following solutions.

$$\begin{aligned}Q_-(t) &= \frac{k_{rec}}{k_{ion}+k_{rec}} + \frac{k_{ion}}{k_{ion}+k_{rec}}e^{-(k_{rec}+k_{ion})t}\\ Q_0(t) &= \frac{k_{ion}}{k_{ion}+k_{rec}} - \frac{k_{ion}}{k_{ion}+k_{rec}}e^{-(k_{rec}+k_{ion})t}\end{aligned} \quad (2)$$

Although the time constant alone is insufficient to separate contributions from NV recombination and ionization, the characteristic rate of both processes impacts the amplitudes of the transient and time-independent components of the response, thus allowing us to extract either rate from a fit. Extended Data Fig. 2d,e shows the results derived from this method for 520 and 594 nm excitation at different power values. All the rates display quadratic dependence within the probed range,

consistent with the two-photon nature of either process[7]. Interestingly, the power dependence of the $NV^- \rightarrow NV^0$ conversion rate of the target due to carrier capture (Fig. 2d, inset) shows a quadratic power dependence as well, which supports the notion that the captured carriers are indeed being photoionized out of a source NV under 520 nm illumination. These measurements give us a precise knowledge of the charge carrier generation rate out of the source NV, an instrumental piece of information for developing and quantifying a model of charge capture by a single defect (as shown below).

Another important piece of information follows from the experiments shown in Extended Data Fig. 3, where we simultaneously monitor the fluorescence response from the NVs (shown in Fig. 2) after laser parks at the source using two different wavelengths. Consistent with the model of cyclic charge generation and transport, we find that 532 nm optical excitation dims the target NV but leaves the source brightness unchanged. Conversely, optical excitation at 632 nm immediately bleaches the source NV but has no impact on the target. An immediate conclusion is that if one was to assume the existence of unaccounted carrier sources, their response to optical excitation of variable wavelengths must be similar to that of an NV.

Local SCC. From the spin-dependent transport experiments shown in Fig. 3, we conclude that a fraction of the carriers that contribute to converting the charge state of the target defect originate from the source NV. To quantitatively determine how large this fraction is, we conduct local SCC measurements at the source NV site following the protocol shown in Extended Data Fig. 4b. Our protocol relies on simultaneous green and red excitation to excite and subsequently trigger the ionization of NV^-, as described previously[35]. We empirically adjust the relative powers for optimal SCC contrast as the process involves a subtle interplay between NV ionization and recombination. Importantly, the SCC pulse is identical (that is, same duration and laser powers) to that used in Fig. 3. Extended Data Fig. 4c shows the source NV response as a function of MW frequency: consistent with prior SCC work in individual NVs[21], we attain a conversion contrast of ~30%.

To correlate this result with earlier observations (Fig. 3d), we first note that because an NV centre—either in the neutral or negative state—undergoes a charge conversion cycle during optical excitation, the emission of a free electron on NV^- ionization must be necessarily compensated with the injection of a hole during NV^0 recombination. Correspondingly, the fluorescence change in the target reflects the contrast attained locally at the source on the completion of a single SCC cycle (even if the overall signal-to-noise ratio decreases due to the probabilistic nature of the carrier exchange between NVs[38]). In particular, comparison with the contrast obtained in Fig. 3 (reaching up to ~20–25%) implies that a fraction greater than 75% of the charge carriers that are trapped by the target NV are photoionized out of the source NV. We stress that this is a lower bound; future work—for example, in the form of experiments at variable excitation wavelengths—will allow us to set a more precise correspondence and, if present, shed light on the nature of any parasitic source.

Carrier transport between few-NV islands. The observations shown in Figs. 2 and 3 are not exclusive to individual NVs. An example is shown in Extended Data Fig. 5, where we investigate the transport between sites comprising two and three NVs (bottom and top circles in Extended Data Fig. 5a, respectively). As observed for single NVs (and ensembles[9]), prolonged green laser parking at the source site (protocol shown in Fig. 2b) leads to the gradual bleaching of NVs at the target site (Extended Data Fig. 5b). By the same token, the application of SCC (Fig. 3a) allows us to encode the (common) spin state of the source NVs into the (common) charge state of the target set; further, by varying the MW frequency, we reconstruct a charge-encoded magnetic resonance spectrum of the source, analogous to that observed in Fig. 3d.

Impact of externally applied electric fields. Although the experiments discussed in the main text rely on carrier self-diffusion from the point of injection, the application of external electric fields should allow us to gain some degree of control over the transport process. To explore this possibility, we pattern metal electrodes on the sample substrate in the form of metal pads separated by a 500 μm gap; the system is oriented so that the resulting electric field **E** is parallel to the line connecting the source and target NVs (Extended Data Fig. 6a). To gauge the impact of the field on the inter-NV carrier transport, we implement a protocol analogous to that shown in Fig. 2, but it is adapted to include a voltage pulse of variable amplitude synchronous with the green laser park (Extended Data Fig. 6b). Extended Data Fig. 6c displays the target NV response as a function of the laser park duration for different voltages. Greater fields gradually lead to slower fluorescence-bleaching rates, hence indicating the progressive blocking of carrier transport from the source; in particular, we observe no change in the target NV charge state for voltages above ~60 V (corresponding to electric fields $E \approx 120\,\mathrm{mV\,\mu m^{-1}}$).

Throughout these measurements, we also observe strong hysteresis in the system response that can be attributed to space-charge fields stemming from the accumulation of trapped carriers at the interface with the electrodes. Recent experiments show that these fields can be fairly strong—exceeding several volts per micrometre—though their exact amplitude and spatial geometry sensitively depend on the relative timing and wavelength of the laser (or lasers) used for photoionization[36]. In particular, we have already shown that these fields can be exploited for carrier guiding[36], though additional work will be needed to gain a fuller understanding.

Extracting the NV^- hole capture cross-section. In the presence of sustained carrier injection from the source, the charge-state dynamics of the target NV can be cast as

$$\frac{dQ_-^{(tar)}}{dt} = \rho_h \xi_h Q_-^{(tar)}, \tag{3}$$

where ρ_h is the hole density at the target site, ξ_h is the NV^- hole capture coefficient, and we have neglected the trapping of electrons by NV^0. Assuming radial hole injection from the source at rate k_h, charge conservation arguments allow us to express the hole density at the target site as

$$\rho_h = \frac{k_h}{4\pi d^2 v_h}, \tag{4}$$

where d denotes the source–target distance and v_h is the hole velocity. Since $\xi_h = \sigma_h v_h$, that is, the product between the NV^- hole capture cross-section σ_h and hole velocity v_h, we write the solution to equation (3) as $Q_-^{(tar)}(t) = Q_-^{(tar)}(0)\, e^{-t/\tau}$, where $Q_-^{(tar)}(0) \approx 0.75$ and

$$\tau = \frac{4\pi d^2}{\sigma_h}\left(\frac{1}{k_{ion}} + \frac{1}{k_{rec}}\right) \tag{5}$$

represents the target NV^- ionization time constant in the presence of hole transport. In equation (5), we assume the hole injection rate is given by $k_h \approx \left(\frac{1}{k_{ion}} + \frac{1}{k_{rec}}\right)^{-1}$ (roughly, the inverse of the time needed for a full cycle of NV ionization and recombination). Since k_{ion} and k_{rec} under 532 nm illumination are known to be quadratic functions of the laser power (Extended Data Fig. 2d), we use equation (5) to simultaneously fit the target NV^- response observed in Figs. 2d and 4c. We obtain $\sigma_h \approx 3 \times 10^{-3}\,\mu m^2$, orders of magnitude greater than typical values reported for ensemble measurements in comparable systems[41].

An arguably more intuitive interpretation of our results emerges from considering the number of emitted holes necessary to induce the bleaching of target fluorescence. For example, from Extended Data Fig. 2d, we roughly estimate the hole injection rate as $\sim 10^6\,s^{-1}$ at 2 mW of 520 nm laser (being the slower of the two, the ionization rate determines the overall rate of the cycle comprising optical ionization and recombination). On the other hand, the charge-state conversion time by the target NV under 2 mW and 520 nm laser illumination of the source is ~0.1 s (Fig. 2d). Therefore, we conclude that one hole is captured by the target NV out of 10^5 holes emitted by the source NV during the charge transfer protocol. For an inter-defect distance of ~4 μm (the example case shown in Fig. 2), this ~10 ppm fraction roughly amounts to the capture cross-section calculated above.

Last, we mention that the presence of charge traps other than the target NV—ignored in the calculations above—can only extend the time required to observe hole capture by the target, implying that the calculated cross-section must be seen as a lower bound. On the other hand, we have observed that optical excitation at sites other than those implanted has no effect on the fluorescence of the target NV, hence suggesting the overall concentration of charge traps is low (at least, in terms of the impact that they have in the present experiments). Additional work will be needed, however, to attain a quantitative estimate.

Model of hole capture by NV^-. Following ref. [40], we hypothesize the capture of a hole by NV^- in diamond starts with the transient formation of a bound exciton state in which the hole occupies an outer hydrogenic orbit centred at the negatively charged defect (Extended Data Fig. 7). The existence of such bound exciton states has already been exposed in SiV^- centres in diamond via optical spectroscopy[39]; as shown by our ab initio calculations, they should also be present in the case at hand (as shown below).

In the simplest representation, the Hamiltonian for an NV^--bound exciton reads

$$H = -\frac{\hbar^2}{2m^*}\nabla^2 - \frac{e^2}{4\pi\varepsilon r}, \tag{6}$$

where m^* denotes the effective mass of the hole, ħ is Planck's constant divided by 2π and ε is the dielectric constant of diamond. Diagonalization of this Hamiltonian leads to the hydrogenic series of energy states given by

$$E_n = E_I - \frac{\varepsilon_0^2}{\varepsilon^2}\frac{m^*}{m_e}\frac{E_{Ry}}{n^2}, \tag{7}$$

where E_I represents the ionization energy, $E_{Ry} = 13.6\,eV$ is the Rydberg energy and m_e is the free electron mass. Qualitatively, one would anticipate hole capture when $E_I - E_n \approx \kappa_B T$, which translates into the Onsager trapping radius

$$r_t = \frac{e^2}{(4\pi\varepsilon\kappa_B T)}. \tag{8}$$

In the above formula, we made use of the expression $r_n = \frac{\varepsilon}{\varepsilon_0}\frac{m_e}{m^*}n^2 a_0$ for the effective radius of the nth orbital, with $a_0 = 0.053$ nm denoting the Bohr radius[53]. Notice that the orbital radii grow with the dielectric constant and inversely depend on the effective carrier mass, which renders r_t ultimately insensitive to m^*.

Using density functional theory (DFT) calculations at the HSE06 level as outlined below, we determine $E_I = 2.71$ eV and $\varepsilon = 5.83\varepsilon_0$. For the effective masses of the hole that can be present either in the light-hole (lh), heavy-hole (hh) or split-off (so) configurations, we use values reported previously[54,55], namely, $m_{hh}^{[111]} = 0.788m_e$, $m_{hh}^{[100]} = 0.366m_e$, $m_{hh}^{[110]} = 1.783m_e$, $m_{lh}^{[111]} = 0.788m_e$, $m_{lh}^{[100]} = 0.366m_e$, $m_{lh}^{[110]} = 0.366m_e$, $m_{so}^{[111]} = 0.198m_e$, $m_{so}^{[100]} = 0.466m_e$ and $m_{so}^{[110]} = 0.232m_e$. In Extended Data Table 1, we show the corresponding values for the excitation energy and the radii exemplified along the [110] direction. For the room-temperature Onsager radius, we obtain $r_t \approx 10$ nm and correspondingly estimate the hole capture cross-section as $\sigma_{h,On} \approx \pi r_t^2 \approx 3\times10^{-4}\,\mu m^2$, within an order of magnitude of the observed value ($\sigma_h = (3\pm1)\times10^{-3}\,\mu m^2$).

A more rigorous approach to determining the hole capture cross-section is the cascade trapping framework[40,56]. Building on a semiclassical picture, this model describes a process in which the energy accrued by the carrier as it accelerates towards the charged defect at the core is released via the emission of consecutive phonons[57]. The Lax model identifies two different regimes: in the Thompson limit, the underlying assumption is that the carrier mean free path is long compared with the characteristic trapping distance $2r_t$, so that one or fewer collisions of the hole occur close to the negative charge centre before the cascade process. By contrast, in the Langevin limit, the free carrier dynamics is diffusive, that is, many collisions occur close to the charge centre.

First, assuming that the Thompson regime applies, we consider two alternative cases where the cascade process is dominated by either acoustic or optical phonons; the latter should be dominant at higher temperatures, whereas the former should prevail under cryogenic conditions. Following ref. [40] and under the assumptions of hole mobility[58] of 1,200 $cm^2\,V^{-1}\,s^{-1}$, speed of sound in diamond[59] of 16,000 $m\,s^{-1}$ and the effective hole masses introduced above, we find that the acoustic-phonon-driven capture cross-section has a value of $\sigma_{h,Th}^{ac} = 1.7\times10^{-6}\,\mu m^2$. Analogously, for the case of scattering by optical phonons, we obtain $\sigma_{h,Th}^{op} = 1.2\times10^{-5}\,\mu m^2$, which should be valid at room temperature. Here we employed $\hbar\omega_{op} = 165$ meV as the corresponding optical phonon energy[60]. Although both results are considerably lower than the experimental value, we note that a formalism where semiclassical trajectories are replaced by a distribution function would likely yield greater cross-sections[56].

Finally, we can also use Lax's framework to derive a capture cross-section valid for the Langevin regime: we obtain $\sigma_{h,La} = 4.35\times10^{-3}\,\mu m^2$, consistent with the experimental result. Although the close agreement might be partly serendipitous, this regime seems justified given the known phonon-scattering rates for carriers in room-temperature diamond[42,43] (of the order of ~$7.5\times10^{12}\,s^{-1}$) corresponding to a mean free path $l \approx 15$ nm comparable to the trapping range $2r_t$.

To characterize the NV-bound excitons in diamond from first-principles calculations, we use spin-polarized DFT calculations as implemented in the Vienna ab initio simulation package (v. 6.1.0) code[61] with the PBE[62] and HSE06[63] exchange–correlation functionals. For the PBE functional, we consider seven different diamond supercells comprising 4,096, 2,744, 1,728, 1,000, 512, 216 and 64 atoms. These supercells have been created by converging the cubic diamond unit cell containing eight atoms with $12\times12\times12$ k-points leading to a lattice constant of 0.356 nm. Using these values, we construct the supercells including the NV centre and optimize the structures until forces are less than $10^{-3}\,eV\,nm^{-1}$ with a plane-wave energy cutoff of 420 eV. Due to the high computational costs of the HSE06 functional, we optimized the supercells by using 1,000, 512, 216 and 64 atoms on this level of theory. Extended Data Fig. 8a shows the calculated charge transition level of the (−1/0) charge state by using an extrapolation of different supercell sizes. This energy corresponds to the ionization energy of the NV^- centre, as well as to the $n\to\infty$ limit in the exciton model introduced above. For PBE and HSE06, we compare two different situations, namely, with and without a charge correction scheme[64]. On interpolation to an infinite carbon-atom count, we find that the corrected and uncorrected schemes lead to the same (−1/0) charge transition level, namely, 2.05 and 2.71 eV for the PBE and HSE06 functionals, respectively. The HSE06 value is in agreement with the experimental value of 2.6 eV (ref. [7]).

Although the long range of the Coulomb potential makes present computing power insufficient for a full ab initio characterization of the bound exciton dynamics, it is, nonetheless, possible to assess the feasibility of the proposed NV model by investigating the $n=1$ state, where confinement is the largest (Extended Data Fig. 8b). To this end, we follow the Delta SCF method outlined in ref. [39]. The procedure consists of two steps: first, we perform a ground-state total energy calculation for NV^0 to subsequently obtain an excited-state energy by promoting an electron from the delocalized valence bands to a state localized at the NV; the electronic configuration of the localized states resembles the configuration of the NV^- centre. This procedure leads to an ($n=1$)-bound exciton energy of 2.03 eV (PBE) and 2.67 eV (HSE06), both lower than their respective ionization energies (Extended Data Fig 7a).

Despite the present limitations, extensions are possible, for example, in the form of effective models amenable to larger system sizes[65], and more accurate many-body methods, such as Green's functions and Bethe–Salpeter-like calculations[66].

Data availability

The data that support the findings of this study are available from the corresponding author upon reasonable request.

Received: 15 May 2021; Accepted: 14 September 2021;
Published online: 22 October 2021

References

1. Degen, C. L., Reinhard, F. & Cappellaro, P. Quantum sensing. *Rev. Mod. Phys.* **89**, 035002 (2017).
2. Awschalom, D. D., Hanson, R., Wrachtrup, J. & Zhou, B. B. Quantum technologies with optically interfaced solid-state spins. *Nat. Photon.* **12**, 516–527 (2018).
3. Atatüre, M., Englund, D., Vamivakas, N., Lee, S.-Y. & Wrachtrup, J. Material platforms for spin-based photonic quantum technologies. *Nat. Rev. Mater.* **3**, 38–51 (2018).
4. Doherty, M. W. et al. The nitrogen-vacancy colour centre in diamond. *Phys. Rep.* **528**, 1–45 (2013).
5. Koehl, W. F., Buckley, B. B., Heremans, F. J., Calusine, G. & Awschalom, D. D. Room temperature coherent control of defect spin qubits in silicon carbide. *Nature* **479**, 84–87 (2011).
6. Tran, T. T., Bray, K., Ford, M. J., Toth, M. & Aharonovich, I. Quantum emission from hexagonal boron nitride monolayers. *Nat. Nanotechnol.* **11**, 37–41 (2015).
7. Aslam, N., Waldherr, G., Neumann, P., Jelezko, F. & Wrachtrup, J. Photo-induced ionization dynamics of the nitrogen vacancy defect in diamond investigated by single-shot charge state detection. *New J. Phys.* **15**, 013064 (2013).
8. Jayakumar, H. et al. Optical patterning of trapped charge in nitrogen-doped diamond. *Nat. Commun.* **7**, 12660 (2016).
9. Dhomkar, S., Zangara, P., Henshaw, J. & Meriles, C. A. On-demand generation of neutral and negatively charged silicon-vacancy centres in diamond. *Phys. Rev. Lett.* **120**, 117401 (2018).
10. Wolfowicz, G. et al. Optical charge state control of spin defects in 4H-SiC. *Nat. Commun.* **8**, 1876 (2017).
11. Widmann, M. et al. Electrical charge state manipulation of single silicon vacancies in a silicon carbide quantum optoelectronic device. *Nano Lett.* **19**, 7173–7180 (2019).
12. Dhomkar, S., Jayakumar, H., Zangara, P. R. & Meriles, C. A. Charge dynamics in near-surface, variable-density ensembles of nitrogen-vacancy centres in diamond. *Nano Lett.* **18**, 4046–4052 (2018).
13. Bluvstein, D., Zhang, Z. & Bleszynski Jayich, A. C. Identifying and mitigating charge instabilities in shallow diamond nitrogen-vacancy centres. *Phys. Rev. Lett.* **122**, 076101 (2019).
14. Siyushev, P. et al. Optically controlled switching of the charge state of a single nitrogen-vacancy centre in diamond at cryogenic temperatures. *Phys. Rev. Lett.* **110**, 167402 (2013).
15. Anderson, C. P. et al. Electrical and optical control of single spins integrated in scalable semiconductor devices. *Science* **366**, 1225–1230 (2019).
16. Wolfowicz, G., Whiteley, S. J. & Awschalom, D. D. Electrometry by optical charge conversion of deep defects in 4H-SiC. *Proc. Natl Acad. Sci. USA* **115**, 7879–7883 (2018).
17. Han, K. Y., Kim, S. K., Eggeling, C. & Hell, S. W. Metastable dark states enable ground state depletion microscopy of nitrogen vacancy centres in diamond with diffraction-unlimited resolution. *Nano Lett.* **10**, 3199–3203 (2010).
18. Chen, X. et al. Subdiffraction optical manipulation of the charge state of nitrogen vacancy centre in diamond. *Light Sci. Appl.* **4**, e230 (2015).
19. Bassett, L. C., Heremans, F. J., Yale, C. G., Buckley, B. B. & Awschalom, D. D. Electrical tuning of single nitrogen-vacancy centre optical transitions enhanced by photo-induced fields. *Phys. Rev. Lett.* **107**, 266403 (2011).
20. Mizuochi, N. et al. Electrically driven single-photon source at room temperature in diamond. *Nat. Photon.* **6**, 299–303 (2012).
21. Shields, B. J., Unterreithmeier, Q. P., De Leon, N. P., Park, H. & Lukin, M. D. Efficient readout of a single spin state in diamond via spin-to-charge conversion. *Phys. Rev. Lett.* **114**, 136402 (2015).
22. Hopper, D. A., Lauigan, J. D., Huang, T.-Y. & Bassett, L. C. Real-time charge initialization of diamond nitrogen-vacancy centers for enhanced spin readout. *Phys. Rev. Appl.* **13**, 024016 (2020).
23. Hopper, D. A., Grote, R. R., Parks, S. M. & Bassett, L. C. Amplified sensitivity of nitrogen-vacancy spins in nanodiamonds using all-optical charge readout. *ACS Nano* **12**, 4678–4686 (2018).
24. Pfender, M. et al. Protecting a diamond quantum memory by charge state control. *Nano Lett.* **17**, 5931–5937 (2017).

25. Dhomkar, S., Henshaw, J., Jayakumar, H. & Meriles, C. A. Long-term data storage in diamond. *Sci. Adv.* **2**, e1600911 (2016).
26. Bourgeois, E. et al. Photoelectric detection of electron spin resonance of nitrogen-vacancy centres in diamond. *Nat. Commun.* **6**, 8577 (2015).
27. Siyushev, P. et al. Photoelectrical imaging and coherent spin-state readout of single nitrogen-vacancy centers in diamond. *Science* **363**, 728–731 (2019).
28. Hrubesch, F. M., Braunbeck, G., Stutzmann, M., Reinhard, F. & Brandt, M. S. Efficient electrical spin readout of NV^- centers in diamond. *Phys. Rev. Lett.* **118**, 037601 (2017).
29. Niethammer, M. et al. Coherent electrical readout of defect spins in silicon carbide by photo-ionization at ambient conditions. *Nat. Commun.* **10**, 5569 (2019).
30. Dolde, F. et al. Nanoscale detection of a single fundamental charge in ambient conditions using the NV^- centre in diamond. *Phys. Rev. Lett.* **112**, 097603 (2014).
31. Doherty, M. W. et al. Towards a room-temperature spin quantum bus in diamond via optical spin injection, transport and detection. *Phys. Rev. X* **6**, 041035 (2016).
32. Chu, Y. et al. Coherent optical transitions in implanted nitrogen vacancy centres. *Nano Lett.* **14**, 1982–1986 (2014).
33. Pezzagna, S., Naydenov, B., Jelezko, F., Wrachtrup, J. & Meijer, J. Creation efficiency of nitrogen-vacancy centres in diamond. *New J. Phys.* **12**, 065017 (2010).
34. Lozovoi, A., Daw, D., Jayakumar, H. & Meriles, C. A. Dark defect charge dynamics in bulk chemical-vapor-deposition-grown diamonds probed via nitrogen vacancy centres. *Phys. Rev. Mater.* **4**, 053602 (2020).
35. Jayakumar, H., Dhomkar, S., Henshaw, J. & Meriles, C. A. Spin readout via spin-to-charge conversion in bulk diamond nitrogen-vacancy ensembles. *Appl. Phys. Lett.* **113**, 122404 (2018).
36. Lozovoi, A., Jayakumar, H., Daw, D., Lakra, A. & Meriles, C. A. Probing metastable space-charge potentials in a wide bandgap semiconductor. *Phys. Rev. Lett.* **125**, 256602 (2020).
37. Hopper, D. A., Grote, R. R., Exarhos, A. L. & Bassett, L. C. Near-infrared-assisted charge control and spin readout of the nitrogen-vacancy centre in diamond. *Phys. Rev. B* **94**, 241201 (2016).
38. Jayakumar, H., Lozovoi, A., Daw, D. & Meriles, C. A. Long-term spin state storage using ancilla charge memories. *Phys. Rev. Lett.* **125**, 236601 (2020).
39. Zhang, Z.-H. et al. Optically detected magnetic resonance in neutral silicon vacancy centres in diamond via bound exciton states. *Phys. Rev. Lett.* **125**, 237402 (2020).
40. Lax, M. Cascade capture of electrons in solids. *Phys. Rev.* **119**, 1502 (1960).
41. Alkauskas, A., Yan, Q. & Van de Walle, C. G. First-principles theory of non-radiative carrier capture via multi-phonon emission. *Phys. Rev. B* **90**, 075202 (2014).
42. Jacoboni, C. & Reggiani, L. The Monte Carlo method for the solution of charge transport in semiconductors with applications to covalent materials. *Rev. Mod. Phys.* **55**, 645 (1983).
43. Suntornwipat, N. et al. A valleytronic diamond transistor: electrostatic control of valley currents and charge-state manipulation of NV centers. *Nano Lett.* **21**, 868–874 (2021).
44. Restrepo, O. D. & Windl, W. Full first-principles theory of spin relaxation in group-IV materials. *Phys. Rev. Lett.* **109**, 166604 (2012).
45. Tamarat, P. et al. Spin-flip and spin-conserving optical transitions of the nitrogen-vacancy centre in diamond. *New J. Phys.* **10**, 045004 (2008).
46. Kazimierczuk, T., Fröhlich, D., Scheel, S., Stolz, H. & Bayer, M. Giant Rydberg excitons in the copper oxide Cu_2O. *Nature* **514**, 343–347 (2014).
47. Irber, D. M. et al. Robust all-optical single-shot readout of NV centers in diamond. *Nat. Commun.* **12**, 532 (2021).
48. Williams, J. R., Low, T., Lundstrom, M. S. & Marcus, C. M. Gate-controlled guiding of electrons in graphene. *Nat. Nanotechnol.* **6**, 222–225 (2011).
49. Sivan, U., Heiblum, M., Umbach, C. P. & Shtrikman, H. Electrostatic electron lens in the ballistic regime. *Phys. Rev. B* **41**, 7937 (1990).
50. Chen, S., Raha, M., Phenicie, C. M., Ourari, S. & Thompson, J. D. Parallel single-shot measurement and coherent control of solid-state spins below the diffraction limit. *Science* **370**, 592–595 (2020).
51. Rose, B. C. et al. Observation of an environmentally insensitive solid-state spin defect in diamond. *Science* **361**, 60–63 (2018).
52. Ziegler, J. F., Ziegler, M. D. & Biersack, J. P. SRIM–the stopping and range of ions in matter (2010). *Nucl. Instrum. Methods B* **268**, 1818–1823 (2010).
53. Albrecht, U. & Bässler, H. Langevin-type charge carrier recombination in a disordered hopping system. *Phys. Status Solidi B* **191**, 455–459 (1995).
54. Willatzen, M., Cardona, M. & Christensen, N. E. Linear muffin-tin-orbital and k·p calculations of effective masses and band structure of semiconducting diamond. *Phys. Rev. B* **50**, 18054 (1994).
55. Löfås, H., Grigoriev, A., Isberg, J. & Ahuja, R. Effective masses and electronic structure of diamond including electron correlation effects in first principles calculations using the GW-approximation. *AIP Adv.* **1**, 032139 (2011).
56. Hamann, D. R. & McWhorter, A. L. Cascade capture of electrons by ionized impurities. *Phys. Rev.* **134**, A250 (1964).
57. Mei, D.-M. et al. Impact of charge trapping on the energy resolution of Ge detectors for rare-event physics searches. *J. Phys. G* **47**, 105106 (2020).
58. Nebel, C. E. Electronic properties of CVD diamond. *Semicond. Sci. Technol.* **18**, S1 (2003).
59. MacQuarrie, E. R., Gosavi, T. A., Jungwirth, N. R., Bhave, S. A. & Fuchs, G. D. Mechanical spin control of nitrogen-vacancy centres in diamond. *Phys. Rev. Lett.* **111**, 227602 (2013).
60. Klein, C. A., Hartnett, T. M. & Robinson, C. J. Critical-point phonon frequencies of diamond. *Phys. Rev. B* **45**, 12854 (1992).
61. Kresse, G. & Furthmüller, J. Efficient iterative schemes for ab initio total-energy calculations using a plane-wave basis set. *Phys. Rev. B* **54**, 11169 (1996).
62. Perdew, J., Burke, K. & Ernzerhof, M. Generalized gradient approximation made simple. *Phys. Rev. Lett.* **77**, 3865 (1996).
63. Krukau, A. V., Vydrov, O. A., Izmaylov, A. F. & Scuseria, G. E. Influence of the exchange screening parameter on the performance of screened hybrid functionals. *J. Chem. Phys.* **125**, 224106 (2006).
64. Freysoldt, C., Neugebauer, J. & VandeWalle, C. G. Fully ab-initio finite-size corrections for charged-defect supercell calculations. *Phys. Rev. Lett.* **102**, 016402 (2009).
65. Ridolfi, E., Lewenkopf, C. H. & Pereira, V. M. Excitonic structure of the optical conductivity in MoS_2 monolayers. *Phys. Rev. B* **97**, 205409 (2018).
66. Refaely-Abramson, S., Qiu, D. Y., Louie, S. G. & Neaton, J. B. Defect-induced modification of low-lying excitons and valley selectivity in monolayer transition metal dichalcogenides. *Phys. Rev. Lett.* **121**, 167402 (2018).

Acknowledgements

We acknowledge useful discussions with Y. H. Chen. A.L., H.J. and C.A.M. acknowledge support from the National Science Foundation through grant no. NSF-1914945, and from Research Corporation for Science Advancement through a FRED award; they also acknowledge access to the facilities and research infrastructure of the NSF CREST IDEALS, grant no. NSF-HRD-1547830. M.W.D. acknowledges support from the Australian Research Council COE170100169. Ion implantation work to generate the NV and SiV centres was performed, in part, at the Centre for Integrated Nanotechnologies, an Office of Science User Facility operated for the US Department of Energy (DOE) Office of Science. Sandia National Laboratories is a multimission laboratory managed and operated by the National Technology and Engineering Solutions of Sandia, LLC, a wholly owned subsidiary of Honeywell International, for the US DOE's National Nuclear Security Administration under contract DE-NA0003525. This paper describes objective technical results and analysis; any subjective views or opinions that might be expressed in the paper do not necessarily represent the views of the DOE or the US Government. The Flatiron Institute is a division of the Simons Foundation.

Author contributions

A.L., H.J. and C.A.M. conceived the experiments. G.V. and E.B. ion implanted the sample. A.L. conducted the experiments and analysed the data with assistance from H.J., D.D. and C.A.M. J.F. led the theoretical and numerical modelling with assistance from M.W.D. C.A.M., A.L. and J.F. wrote the manuscript with input from all the authors. C.A.M. supervised the project.

Competing interests

The authors declare no competing interests.

Additional information

Extended data is available for this paper at https://doi.org/10.1038/s41928-021-00656-z.

Correspondence and requests for materials should be addressed to Carlos A. Meriles.

Peer review information *Nature Electronics* thanks Sang-Yun Lee and the other, anonymous, reviewer(s) for their contribution to the peer review of this work.

Reprints and permissions information is available at www.nature.com/reprints.

Publisher's note Springer Nature remains neutral with regard to jurisdictional claims in published maps and institutional affiliations.

© The Author(s), under exclusive licence to Springer Nature Limited 2021

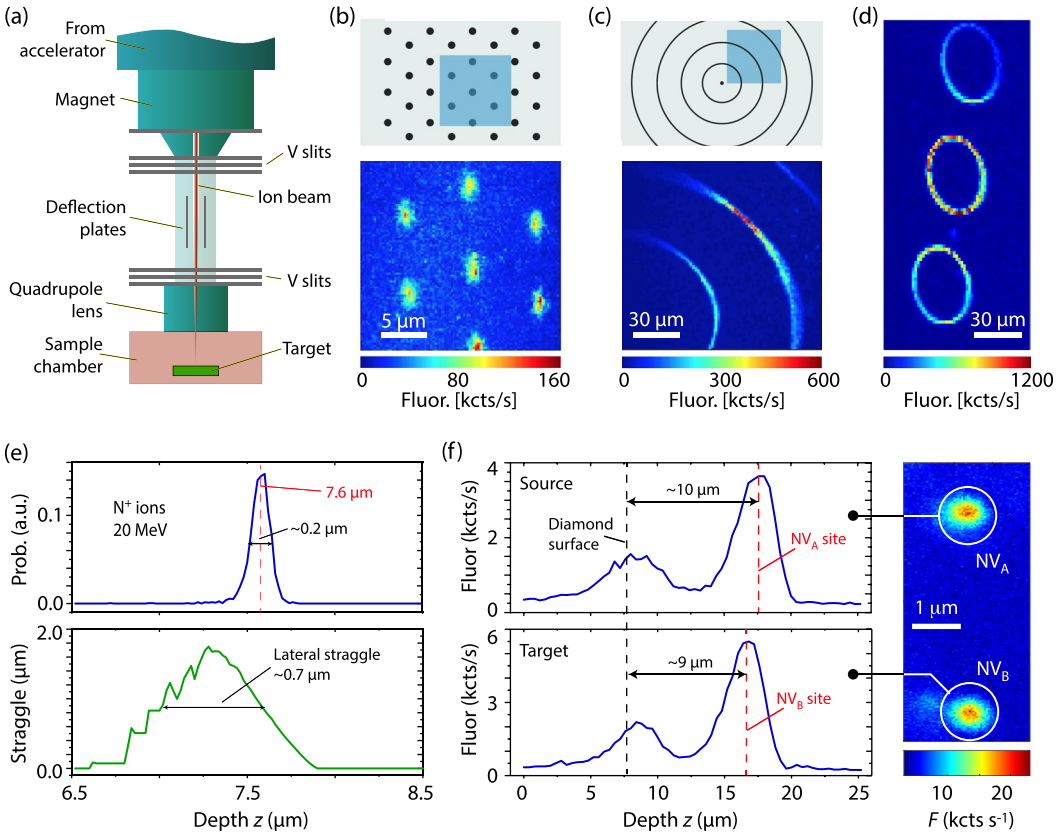

Extended Data Fig. 1 | Engineering deep NV arrays via a high-energy focused ion beam. (a) Schematics of the ion implanter. (b-d) Example NV patterns; fluorescence images in **(b)** and **(c)** correspond to the shaded areas in the larger NV arrays (upper schematics). **(e)** SRIM simulations assuming an implantation energy of 20 MeV; the top and bottom plots are the number probability distribution and lateral ion straggle as a function of depth, respectively. **(f)** NV fluorescence intensity as a function of depth for the source and target single NVs in Fig. 1c of the main text (top and bottom plots, respectively).

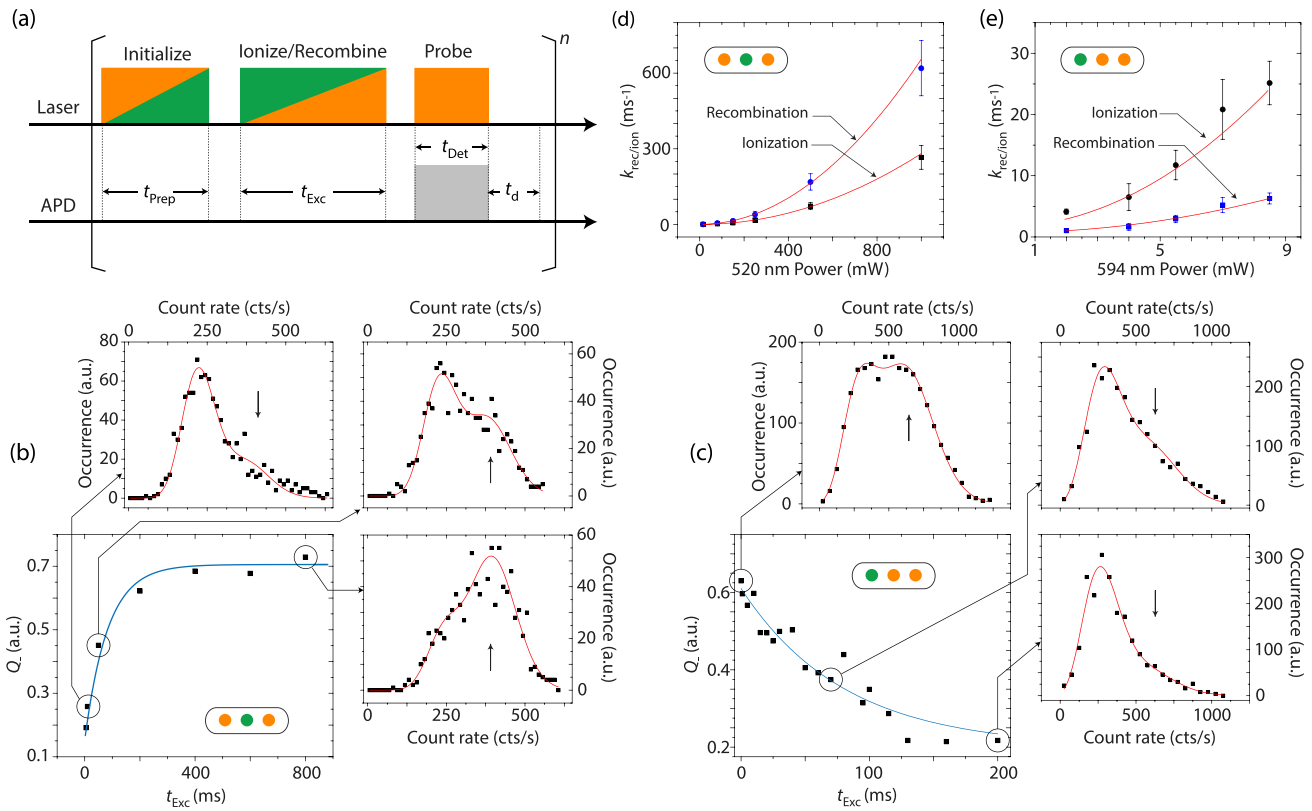

Extended Data Fig. 2 | Charge control of individual NVs. (a) Experimental protocol. Green (orange) blocks indicate laser excitation at 520 nm (594 nm). Left (right) triangles apply to the NV^- recombination (ionization) measurements. APD denotes the avalanche photo-detector. **(b)** Relative NV^- population as a function of the excitation time t_{Exc} for 520 nm, 35 μW laser light; the solid trace is an exponential fit and the color code in the lower right corner indicates the laser color sequence. Surrounding plots are example histograms for different values of t_{Exc}, with solid red traces indicating fits corresponding to two Poissonian distributions with differing average count rates. Black arrows indicate contributions due to NV^-; both ionization and recombination rates at the excitation wavelength and power can be extracted from these fits (see text for details). During initialization, the orange laser power and duration are 7 μW and 200 ms, respectively; the readout pulse at 594 nm has a power of 7 μW and a duration of 80 ms. **(c)** Relative NV^- population as a function of the excitation time t_{Exc} produced by a 594 nm, 4 μW laser. As in **(b)**, NV^- populations can be extracted from analysis of the recorded histograms. In this protocol, the 520 nm initialization (594 nm readout) pulse has 200 μW (4 μW) power and a duration of 500 μs (20 ms). **(d)** NV recombination and ionization rates k_{rec}, k_{ion} (blue and black dots, respectively) as a function of the 520 nm laser power as extracted from experiments similar to those in **(b)**. Solid red traces indicate parabolic fits. **(e)** Same as in **(d)** but for 594 nm. All experiments are carried out in NV_A ('source' NV in Fig. 2 of the main text). Similar results are obtained for NV_B, not shown here for brevity.

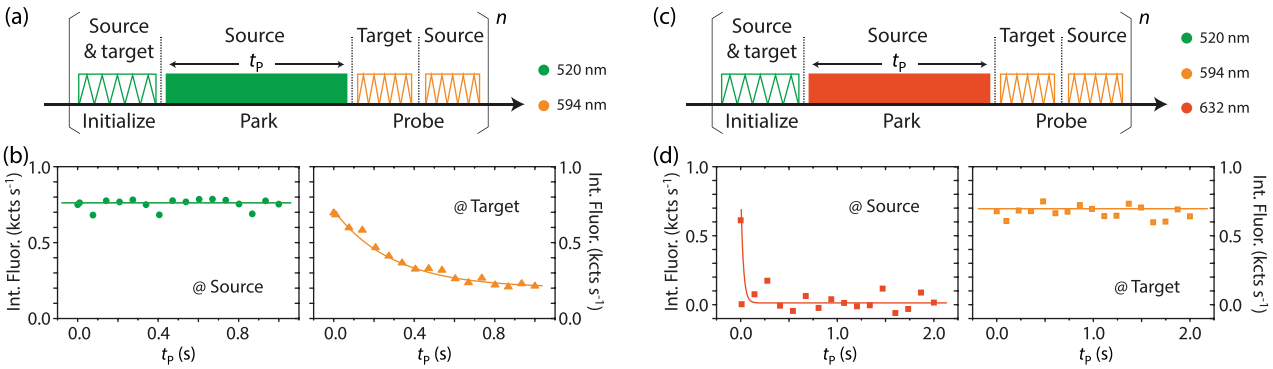

Extended Data Fig. 3 | Source-target carrier transport at different excitation wavelengths. (a) Working with the NV pair presented in Fig. 2 of the main text, we modify the experimental protocol to include a 594 nm fluorescence scan over a 1.5×1.5 μm^2 area around the source NV, which we use to determine its integrated fluorescence. **(b)** Time-averaged, integrated fluorescence of the source and target NVs (left and right panels, respectively); while the former gradually bleaches, the latter remains bright. The 520 nm laser intensity during the park is 1.0 mW; all other conditions as in Fig. 2. **(c)** Same as in **(a)** but using a 1.5 mW, 632 nm park. **(d)** Same as in **(b)** but for the protocol in **(c)**. The source NV transitions immediately to a dark state while the target remains bright. Solid lines in **(b)** and **(d)** are guides to the eye.

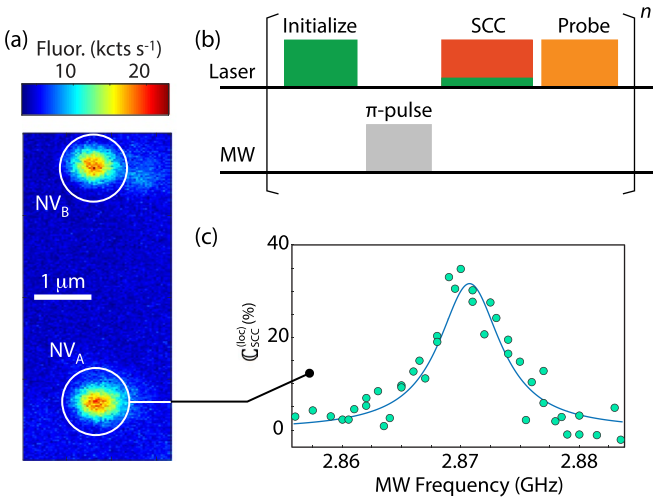

Extended Data Fig. 4 | Local spin-to-charge conversion. (a) Fluorescence image of target and source NVs. **(b)** Spin-to-charge conversion (SCC) protocol. Green, red, and orange blocks indicate laser excitation at 520 nm, 632 nm, and 594 nm, respectively. During SCC, red and green excitation take place simultaneously. The grey block indicates MW excitation at variable frequency; the MW pulse length and amplitude are chosen to induce a population inversion when on-resonance with the NV ground state zero-field splitting (~2.87 GHz). **(c)** Fluorescence change from NV_A (source) as a function of the MW frequency upon application of the SCC protocol in **(b)**. Throughout these experiments, the power and duration of the initialization (probe) pulse are 200 μW and 500 μs (7 μW and 15 ms), respectively. The green (red) laser power during SCC is 200 μW (16 mW); the SCC pulse duration amounts to 300 ns.

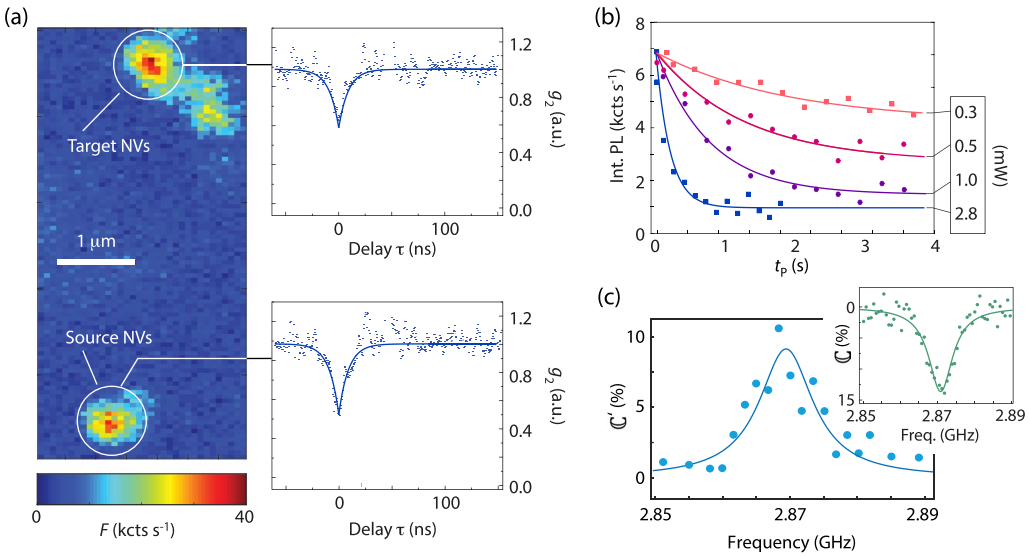

Extended Data Fig. 5 | Transport between few-NV islands. (a) Fluorescence image of two proximal ion implantation spots. Time-correlated single-photon measurements at the circled sites indicate the presence of 2 or 3 NVs at each location. **(b)** NV^- photo-luminescence at the target site upon application of the protocol in Fig. 2b of the main text for variable park times t_p and different laser powers. **(c)** NV^- fluorescence from the target site as a function of the MW frequency upon spin-to-charge conversion at the source site (protocol in Fig. 3a of the main text). As a reference, the insert the displays the optically detected magnetic resonance spectrum of the source NVs. Conditions are similar to those in Figs. 2 and 3 of the main text.

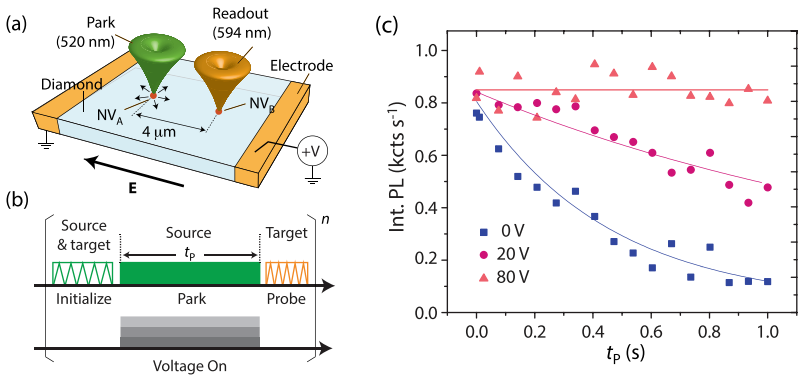

Extended Data Fig. 6 | Inter-NV transport in the presence of externally applied electric fields. (a) Schematics of the experimental setup. We pattern metal pads on the sample substrate to produce an electric field **E** parallel to the axis connecting the source and target NVs (respectively, NV_A and NV_B). The gap between the electrodes is 500 μm. **(b)** Pulse protocol. After NV initialization (green scan at the source and target NVs), we apply a voltage of variable (but fixed) amplitude synchronically with the green laser park at the source NV; we readout the charge state of the target NV via an orange scan. Positive voltages create an electric field pointing from NV_B to NV_A. **(c)** Integrated fluorescence of the target NV as a function of the green laser park time t_P for different voltages. The green laser power during the park is 1 mW; all other conditions as in Fig. 2 of the main text.

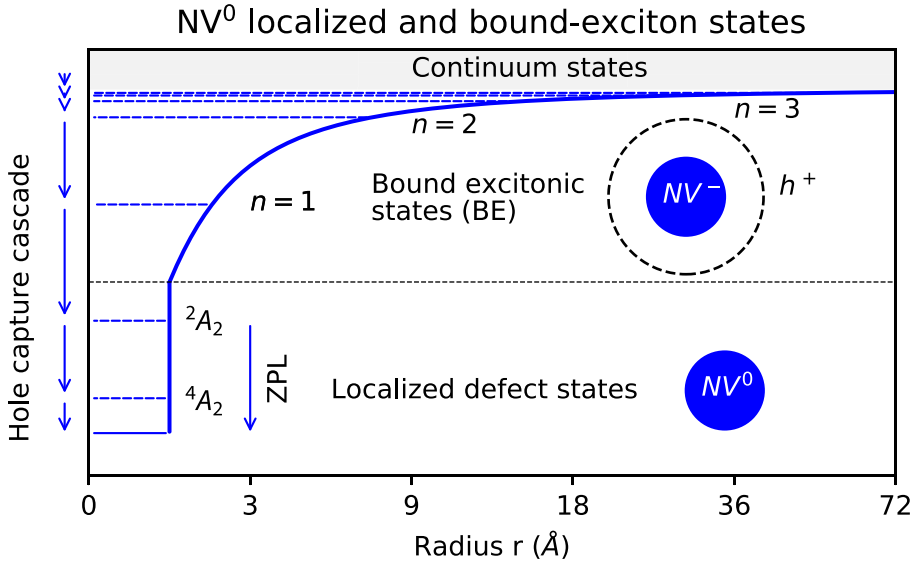

Extended Data Fig. 7 | Cascade capture of a hole by a negatively charged NV. We consider the formation of a bound exciton state comprising a hole orbiting an NV^- core. This system can be described by a hydrogenic series of states characterized by a quantum number n. Assuming the hole is in thermal equilibrium, bound exciton formation is possible for orbits n_t such that $(E_I - E_n) \sim \kappa_B T$; subsequent capture involves the cascade emission of phonons. The corresponding trapping radius (also known as the 'Onsager' radius[53,57]) is given by $r_t = e^2/(4\pi\varepsilon\kappa_B T) \approx 10$ nm in room temperature diamond. The ensuing capture cross-section would then amount to $\sigma_{h,On} \sim 3 \times 10^{-4}\ \mu m^2$, not far off from the experimental value.

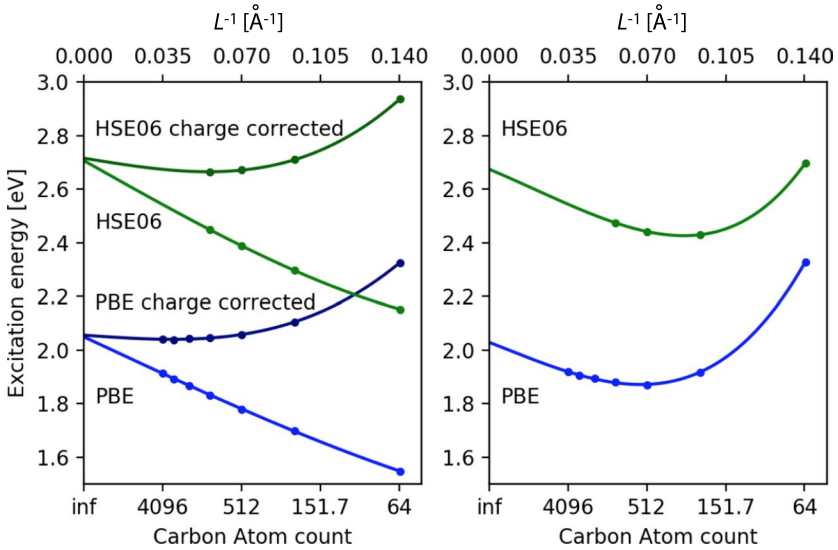

Extended Data Fig. 8 | DFT modeling. (Left) PBE- and HSE06-calculated exchange-correlation functional for the (0/−1) charge transition level (blue and green dots, respectively), which corresponds to the ionization energy of the NV^- center. For each functional, we show two values, the uncorrected (light) and the charge corrected[64] (dark) excitation energies. Both lead to the same value for the extrapolation at infinite carbon atoms in the supercell. (Right) $n = 1$ bound exciton energy using the HSE06 (green) and the PBE (blue) exchange-correlation functional. The solid lines in **(a)** stem from fits using the formula $(x) = a + \left(bx + cx^3\right) \exp(-dx)$, where a, b, c and d are fitting parameters, and $x \equiv L^{-1}$ is the inverse supercell length. All values are listed in Extended Data Table 2.

Extended Data Table 1 | Excitation energies and radii

n	E_n^{lh} (eV)	r_n^{lh} (nm)	E_n^{hh} (eV)	r_n^{hh} (nm)	E_n^{so} (eV)	r_n^{so} (nm)
1	2.564	0.843	1.997	0.173	2.617	1.330
2	2.673	3.372	2.532	0.692	2.690	5.319
3	2.694	7.587	2.631	1.557	2.699	11.969
4	2.700	13.487	2.665	2.769	2.704	21.277

We consider the lowest four bound exciton states along the [110] direction based on Eq. (7).

Extended Data Table 2 | Fitting parameters for the DFT data shown in Extended Data Fig. 8

NV (0, −1) transition energy				
$f(x) = a+(bx+cx^3)$	a (eV)	b (eV Å)	c (eV Å^2)	
PBE	2.05	−3.93	18.03	
PBE (charge corrected)	2.06	−0.59	127.67	
HS06	2.71	−4.74	40.00	
HS06 (charge corrected)	2.72	−1.37	149.67	
n=1 bound exciton energy				
$f(x) = a+(bx+cx^3)\exp(-dx)$	a (eV)	b (eV Å)	c (eV Å^2)	d (eV Å)
PBE	2.03	−3.30	257.44	1.34
HS06	2.67	−3.57	186.27	3.23

In these equations $x \equiv L^{-1}$ is the inverse supercell length.